INTERNATIONAL JOURNAL FOR NUMERICAL METHODS IN FLUIDS, VOL. 21, 933–953 (1995)

PARALLEL FINITE ELEMENT SIMULATION OF 3D INCOMPRESSIBLE FLOWS: FLUID–STRUCTURE INTERACTIONS

S. MITTAL

Aerospace Engineering, II T Kanpur, Kanpur 208016, India

AND

T. E. TEZDUYAR

Aerospace Engineering and Mechanics, Army HPC Research Center, University of Minnesota, Minneapolis, MN 55415, U.S.A.

SUMMARY

Massively parallel finite element computations of 3D, unsteady incompressible flows, including those involving fluid–structure interactions, are presented. The computations with time-varying spatial domains are based on the deforming spatial domain/stabilized space–time (DSD/SST) finite element formulation. The capability to solve 3D problems involving fluid–structure interactions is demonstrated by investigating the dynamics of a flexible cantilevered pipe conveying fluid. Computations of flow past a stationary rectangular wing at Reynolds number 1000, 2500 and 10^7 reveal interesting flow patterns. In these computations, at each time step approximately 3×10^6 non-linear equations are solved to update the flow field. Also, preliminary results are presented for flow past a wing in flapping motion. In this case a specially designed mesh moving scheme is employed to eliminate the need for remeshing. All these computations are carried out on the Army High Performance Computing Research Center supercomputers CM-200 and CM-5, with major speed-ups compared with traditional supercomputers. The coupled equation systems arising from the finite element discretizations of these large-scale problems are solved iteratively with diagonal preconditioners. In some cases, to reduce the memory requirements even further, these iterations are carried out with a matrix-free strategy. The finite element formulations and their parallel implementations assume unstructured meshes.

KEY WORDS: parallel finite elements; 3D incompressible flows; fluid–structure interactions

1. INTRODUCTION

In the past years the availability of massively parallel computers has provided us with the opportunity to carry out large-scale, unsteady, 3D finite element simulations. We present our numerical results, computed on the Army High Performance Computing Research Center (AHPCRC) supercomputers CM-200 and CM-5, for 3D, unsteady flows, including those involving fluid–structure interactions. For problems involving deforming domains, the fluid dynamics equations are solved with a stabilized space–time finite element method. In the space–time formulation the finite element interpolation functions vary both spatially and temporally. It was first shown by Tezduyar *et al.*[1,2] that this stabilized space–time finite element formulation can be effectively applied to fluid dynamics computations involving moving boundaries and interfaces. They successfully applied the DSD/SST (deforming spatial domain/stabilized space–time) procedure they introduced to unsteady incompressible flow problems involving free surfaces, liquid drops, two-liquid interfaces and drifting cylinders. Later Mittal and Tezduyar[3,4] applied this method to simulate flows past moving cylinders and aerofoils. Parallel

CCC 0271–2091/95/100933–21 *Received 19 June 1994*

implementation of the stabilized space–time method is described in the paper by Behr *et al.*[5] along with several example problems. For flow problems involving fixed domains, to save on the CPU time and memory, we use a one-step semidiscrete formulation. To reduce the cost associated with these large-scale computations, iterative solution strategies are employed to solve the coupled equation systems arising from the finite element discretizations of the problems. In these iterations we use a diagonal preconditioner with the GMRES[6] update technique. In some cases, to reduce the memory requirements even further, matrix-free implementation[7] of these iterations is used. The finite element formulations and their parallel implementations employed in this work assume unstructured meshes.

The first problem considered in this paper is the computation of 3D flow in a flexible cantilevered pipe and the response of the pipe to this flow. One of the early works in this area was motivated by the vibration of the Trans-Arabian pipeline. In 1952 Housner[8] investigated this phenomenon based on a simple beam theory for pipes with simply supported ends. He found that for sufficiently high velocities the pipe may buckle, essentially like a column subjected to axial loading. In 1966 Gregory and Paidoussis[9,10] showed, theoretically and experimentally, that cantilevered pipes exhibit a contrasting behaviour compared with pipes with simply supported ends. At sufficiently high flow velocities the cantilevered pipes exhibit oscillatory instabilities rather than buckling. This observation was consistent with that of Benjamin,[11,12] who investigated the dynamics of articulated pipes conveying fluid as a discrete representation of a continuously flexible system. The interested reader is referred to the paper by Paidoussis and Issid[13] for a detailed discussion. In the present work the deformation of the pipe is based on the Bernoulli–Euler beam theory. The governing equations for the fluid flow are solved using the stabilized space–time method, while a Galerkin formulation, in conjunction with the 'α-method' for time integration,[14] is employed for solving the equation of motion for the pipe.

Next, results are presented for flow past a stationary rectangular wing, with NACA 0012 section, at 12·5° angle of attack and at Reynolds number 1000, 2500 and 10^7. Our computations converge to a steady state solution at Reynolds number 1000. As expected, a pair of wing tip vortices is observed in the solution. At Reynolds number 2500 we obtain a temporally periodic solution. At Reynolds number 10^7 we use the Prandtl mixing length model to account for the Reynolds stresses in the turbulent flow. A semidiscrete formulation is employed to carry out these computations. Approximately 3×10^6 non-linear equations are solved at each time step with matrix-free iterations. On a 512-node CM-5 these computations achieve a sustained speed of 10 GFLOPS.

Finally we present results from preliminary computations for flow past a wing in flapping motion. The motion is based on a description given by Lighthill[15] of the flight of birds. From our computations we observe that during one time period (the upstroke and downstroke) this motion of the wing generates a net thrust and lift. A specially designed mesh-moving scheme[3] is employed to handle the motion of the wing without any remeshing. Therefore our solutions are free from projection errors associated with remeshing. Avoiding remeshing also aids us in utilizing the massively parallel machines efficiently.

2. THE GOVERNING EQUATIONS

2.1. *The Navier–Stokes equations*

Let Ω_t in $\mathbb{R}^{n_{sd}}$ be the spatial domain at time $t \in (0, T)$, where n_{sd} is the number of space dimensions. Let Γ_t denote the boundary of Ω_t. We consider the following velocity–pressure formulation of the Navier–Stokes equations governing unsteady incompressible flows:

$$\rho\left(\frac{\partial \mathbf{u}}{\partial t} + \mathbf{u} \cdot \nabla \mathbf{u}\right) - \nabla \cdot \boldsymbol{\sigma} = \mathbf{0} \quad \text{on } \Omega_t \quad \forall t \in (0, T), \tag{1}$$

$$\nabla \cdot \mathbf{u} = 0 \quad \text{on } \Omega_t \quad \forall t \in (0, T), \tag{2}$$

where ρ and $\mathbf{u}$ are the density and velocity respectively and $\boldsymbol{\sigma}$ is the stress tensor given as

$$\boldsymbol{\sigma}(p, \mathbf{u}) = -p\mathbf{I} + 2\mu\boldsymbol{\varepsilon}(\mathbf{u}), \tag{3}$$

with

$$\boldsymbol{\varepsilon}(\mathbf{u}) = \tfrac{1}{2}[\nabla\mathbf{u} + (\nabla\mathbf{u})^T]. \tag{4}$$

Here p and μ are the pressure and dynamic viscosity respectively and $\mathbf{I}$ is the identity tensor. The part of the boundary at which the velocity is assumed to be specified is denoted by $(\Gamma_t)_\mathbf{g}$:

$$\mathbf{u} = \mathbf{g} \quad \text{on } (\Gamma_t)_\mathbf{g} \quad \forall t \in (0, T). \tag{5}$$

The 'natural' boundary conditions associated with (1) are the conditions on the stress components, and these are the conditions assumed to be imposed on the remaining part of the boundary:

$$\mathbf{n} \cdot \sigma = \mathbf{h} \quad \text{on } (\Gamma_t)_\mathbf{h} \quad \forall t \in (0, T). \tag{6}$$

The homogeneous version of (6), which corresponds to the 'traction-free' (i.e. zero normal and shear stress) conditions, is often imposed at the outflow boundaries. As initial condition, a divergence-free velocity field $\mathbf{u}_0(\mathbf{x})$ is specified over the domain Ω_t at $t = 0$:

$$\mathbf{u}(\mathbf{x}, 0) = \mathbf{u}_0(\mathbf{x}) \quad \text{on } \Omega_0. \tag{7}$$

2.2. Equations of motion for a flexible cantilevered pipe

Shown in Figure 1(a) is a schematic diagram of the pipe system under consideration. It consists of a uniform, tubular cantilever of length L, with flexural rigidity EI and mass m per unit length, conveying a stream of incompressible fluid of mass m_f per unit length. The z-axis coincides with the centreline of the undeformed tube, whose transverse deflection x is measured normal to the z-axis. The motion of the pipe is restricted to the x–z plane. Figure 1(b) shows the free-body diagram of a pipe element. Force balance in the z- and x-directions yields the following equations for the pipe:

$$F_z + \frac{\partial T}{\partial z} = 0, \tag{8}$$

$$\frac{\partial Q}{\partial z} + F_x + \frac{\partial}{\partial z}\left(T\frac{\partial x}{\partial z}\right) - m\ddot{x} = 0. \tag{9}$$

Here F_x and F_z are the fluid forces acting on the pipe per unit length, T is the longitudinal tension in the pipe and Q is the transverse force. The shear force Q is related to the bending moment M acting on the pipe by

$$Q = -\frac{\partial M}{\partial z}. \tag{10}$$

For small deflections the bending moment M is related to the lateral deflection by

$$M = EI\frac{\partial^2 x}{\partial z^2}. \tag{11}$$

The longitudinal tension in the pipe is determined by integrating equation (8) along the pipe:

$$T(z) = T(L) + \int_z^L F_z \, \mathrm{d}z, \tag{12}$$

where $T(L)$ is the tension at the free end of the pipe.

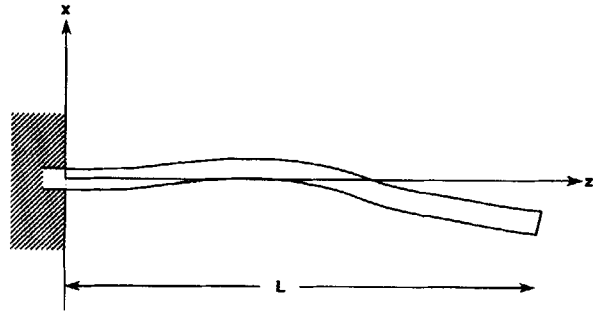

Figure 1(a). Flow in a flexible cantilevered pipe: schematic lay-out

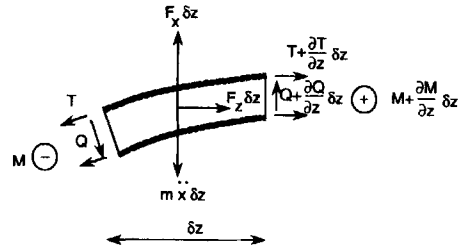

Figure 1(b). Flow in a flexible cantilevered pipe: free-body diagram of a pipe element

Substituting equations (10) and (11) into equation (9), we obtain the equation of motion for the pipe as

$$-EI\frac{\partial^4 x}{\partial z^4} - F_z\frac{\partial x}{\partial z} + F_x + T\frac{\partial^2 x}{\partial z^2} - m\ddot{x} = 0. \tag{13}$$

The boundary conditions for this cantilevered beam correspond to zero deflection and slope at the fixed end and zero bending moment and shear force at the free end:

$$\begin{aligned} x(0,t) &= 0, & \frac{\partial x}{\partial z}(0,t) &= 0, \\ \frac{\partial^2 x}{\partial^2 z}(L,t) &= 0, & \frac{\partial^3 x}{\partial^3 z}(L,t) &= 0. \end{aligned} \tag{14}$$

As initial condition, displacement and velocity fields are specified along the pipe:

$$x(z,0) = x_0, \qquad \dot{x}(z,0) = \dot{x}_0. \tag{15}$$

To cast equation (13) in a non-dimensional form, we define the following dimensionless variables:

$$\begin{aligned} \zeta &= \frac{z}{L}, & \chi &= \frac{x}{L}, & \theta &= \sqrt{\left(\frac{EI}{m_f + m}\right)}\frac{t}{L^2}, \\ C_z &= \frac{F_z L}{m_f U^2}, & C_x &= \frac{F_x L}{m_f U^2}, & C_T &= \frac{T}{m_f U^2}, \end{aligned} \tag{16}$$

where U is the mean flow velocity in the pipe. The non-dimensional form of equation (13) is

$$-\frac{\partial^4 \chi}{\partial \zeta^4} - \bar{u}^2 C_z\frac{\partial \chi}{\partial \zeta} + \bar{u}^2 C_x + \bar{u}^2 C_T\frac{\partial^2 \chi}{\partial \zeta^2} - (1-\beta)\frac{\partial^2 \chi}{\partial \theta^2} = 0. \tag{17}$$

The dimensionless parameters associated with the pipe–fluid system, β and $\bar{u}$, are defined as

$$\beta = \frac{m_f}{m_f + m}, \tag{18}$$

$$\bar{u} = \sqrt{\left(\frac{m_f}{EI}\right)} UL. \tag{19}$$

3. FINITE ELEMENT FORMULATIONS

3.1. The space–time formulation with the Galerkin/least squares stabilization

Our main motiviation for using the space–time formulation is to be able to solve problems that involve moving boundaries and interfaces. In this formulation the finite element interpolation functions vary both spatially and temporally. On the other hand, in semidiscrete finite element formulations the interpolation functions vary only spatially and a finite difference discretization in time is employed for unsteady problems.

In the space–time finite element formulation the time interval $(0, T)$ is partitioned into subintervals $I_n = (t_n, t_{n+1})$, where t_n and t_{n+1} belong to an ordered series of time levels $0 = t_0 < t_1 < \cdots < t_N = T$. In this formulation the spatial domains at various time levels are allowed to vary. We let $\Omega_n = \Omega_{t_n}$ and $\Gamma_n = \Gamma_{t_n}$ and define the space–time slab Q_n as the space–time domain enclosed by the surfaces Ω_n, Ω_{n+1} and P_n. Here P_n, the lateral surface of Q_n, is the surface described by the boundary Γ as t traverses I_n. Similarly to the way it was represented by equations (5) and (6), P_n is decomposed into $(P_n)_{\mathbf{g}}$ and $(P_n)_{\mathbf{h}}$ with respect to the type of boundary condition being imposed.

Finite element discretization of a space–time slab Q_n is achieved by dividing it into elements Q_n^e, $e = 1, 2, \ldots, (n_{el})_n$, where $(n_{el})_n$ is the number of elements in the space–time slab Q_n. Associated with this discretization, for each space–time slab we define the following finite element interpolation function spaces for the velocity and pressure:

$$(S_{\mathbf{u}}^h)_n = \{\mathbf{u}^h | \mathbf{u}^h \in [H^{1h}(Q_n)]^{n_{sd}}, \mathbf{u}^h \doteq \mathbf{g}^h \text{ on } (P_n)_{\mathbf{g}}\}, \tag{20}$$

$$(V_{\mathbf{u}}^h)_n = \{\mathbf{w}^h | \mathbf{w}^h \in [H^{1h}(Q_n)]^{n_{sd}}, \mathbf{w}^h \doteq \mathbf{0} \text{ on } (P_n)_{\mathbf{g}}\}, \tag{21}$$

$$(S_p^h)_n = \{p^h | p^h \in H^{1h}(Q_n)\}, \tag{22}$$

$$(V_p^h)_n = \{q^h | q^h \in H^{1h}(Q_n)\}. \tag{23}$$

Here $H^{1h}(Q_n)$ represents the finite-dimensional function space over the space–time slab Q_n. This space is formed by using, over the parent (element) domains, first-order polynomials in space and time. Similarly to the way one chooses the order of polynomials in space to obtain desired accuracy and convergence, in a space–time formulation one can choose the order of polynomials in time. Whatever the order of the polynomials is, globally the interpolation functions are continuous in space but discontinuous in time.

The space–time formulation of (1)–(7) can be written as follows: start with

$$(\mathbf{u}^h)_0^- = (\mathbf{u}_0)^h; \tag{24}$$

sequentially for $Q_1, Q_2, \ldots, Q_{N-1}$, given $(\mathbf{u}^h)_n^-$, find $\mathbf{u}^h \in (S_{\mathbf{u}}^h)_n$ and $p^h \in (S_p^h)_n$ such that $\forall \mathbf{w}^h \in (V_{\mathbf{u}}^h)_n$ and $\forall q^h \in (V_p^h)_n$

$$\int_{Q_n} \mathbf{w}^h \cdot \rho\left(\frac{\partial \mathbf{u}^h}{\partial t} + \mathbf{u}^h \cdot \nabla \mathbf{u}^h\right) dQ + \int_{Q_n} \boldsymbol{\varepsilon}(\mathbf{w}^h) : \boldsymbol{\sigma}(p^h, \mathbf{u}^h)\, dQ$$

$$- \int_{(P_n)_h} \mathbf{w}^h \cdot \mathbf{h}\, dP + \int_{Q_n} q^h \nabla \cdot \mathbf{u}^h dQ + \int_{\Omega_n} (\mathbf{w}^h)_n^+ \cdot \rho[(\mathbf{u}^h)_n^+ - (\mathbf{u}^h)_n^-]\, d\Omega$$

$$+ \sum_{e=1}^{(n_{el})_n} \int_{Q_n^e} \tau \frac{1}{\rho}\left[\rho\left(\frac{\partial \mathbf{w}^h}{\partial t} + \mathbf{u}^h \cdot \nabla \mathbf{w}^h\right) - \nabla \cdot \boldsymbol{\sigma}(q^h, \mathbf{w}^h)\right] \cdot \left[\rho\left(\frac{\partial \mathbf{u}^h}{\partial t} + \mathbf{u}^h \cdot \nabla \mathbf{u}^h\right) - \nabla \cdot \boldsymbol{\sigma}(p^h, \mathbf{u}^h)\right] dQ$$

$$+ \sum_{e=1}^{(n_{el})_n} \int_{Q_n^e} \delta \nabla \cdot \mathbf{w}^h \rho \nabla \cdot \mathbf{u}^h\, dQ = 0. \tag{25}$$

In the variational formulation given by (25), the following notation is used:

$$(\mathbf{u}^h)_n^{\pm} = \lim_{\delta \to 0} \mathbf{u}^h(t_n \pm \delta), \tag{26}$$

$$\int_{Q_n} (\ldots)\, dQ = \int_{I_n} \int_{\Omega} (\ldots)\, d\Omega\, dt, \tag{27}$$

$$\int_{P_n} (\ldots)\, dP = \int_{I_n} \int_{\Gamma} (\ldots)\, d\Gamma\, dt. \tag{28}$$

The first four integrals in equation (25) correspond to the Galerkin formulation of (1)–(7) in a semidiscrete finite element formulation. The choice of interpolation functions that are discontinuous in time makes it possible in the space–time formulation to solve for the fully discrete equations one space–time slab at a time. The fifth integral in equation (25) enforces, weakly, the continuity of the velocity in time.

To assure the numerical stability of the computations, a series of integrals involving the coefficients τ and δ are added to the Galerkin variational formulation in equation (25). These integrals are obtained by invoking the Galerkin/least squares (GLS) procedure. This procedure is a generalization of the stabilization based on the streamline upwind/Petrov–Galerkin (SUPG) and pressure-stabilizing/Petrov–Galerkin (PSPG) procedures[16] employed for incompressible flows. Such stabilization procedures allow one to use elements which have equal-order interpolation functions for velocity and pressure and which are otherwise unstable. For definitions of the coefficients τ and δ the interested reader is referred to References 3 and 4. A semidiscrete version of this formulation can be used to solve flow problems on fixed domains. In that case the finite element interpolation functions do not depend on time. A finite difference discretization, e.g. the Crank–Nicolson scheme, is utilized along the temporal axis. Furthermore, the fifth integral in equation (25) is dropped from the formulation. It is important to realize that the stabilizing terms added involve the momentum and continuity equations as factors. Therefore, despite these additional terms, an exact solution is still admissible to the variational formulation given by equation (25). Thus in this respect our formulations are consistent.

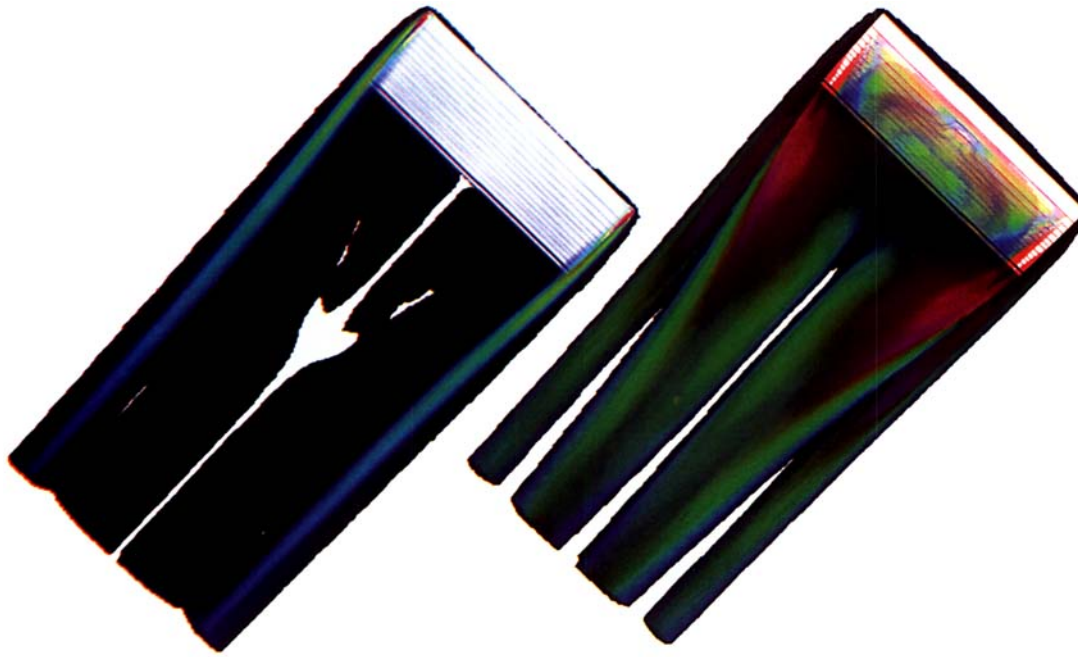

Plate 1. Flow past a stationary rectangular wing at *Re*=1000: magnitudes of helicity (left) and vorticity (right)

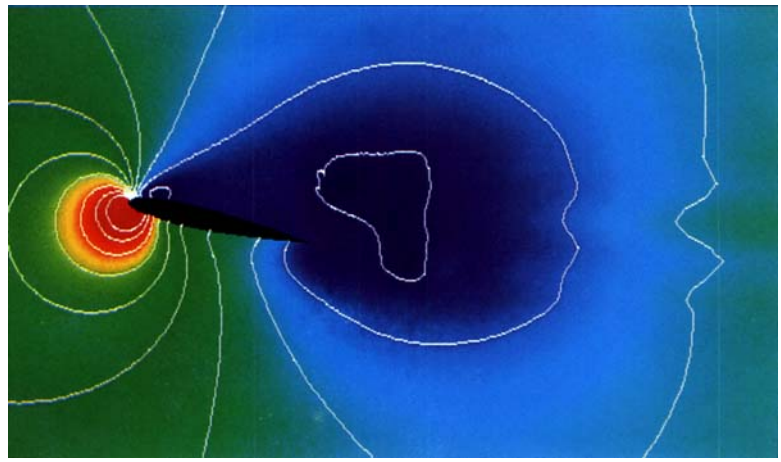

Plate 2. Flow past a stationary rectangular wing at *Re*=1000: pressure in a plane passing through the centre of wing

Plate 3. Flow past a stationary rectangular wing at *Re*=2500: magnitudes of helicity (left) and vorticity (right) at three instants during half a period of vortex shedding

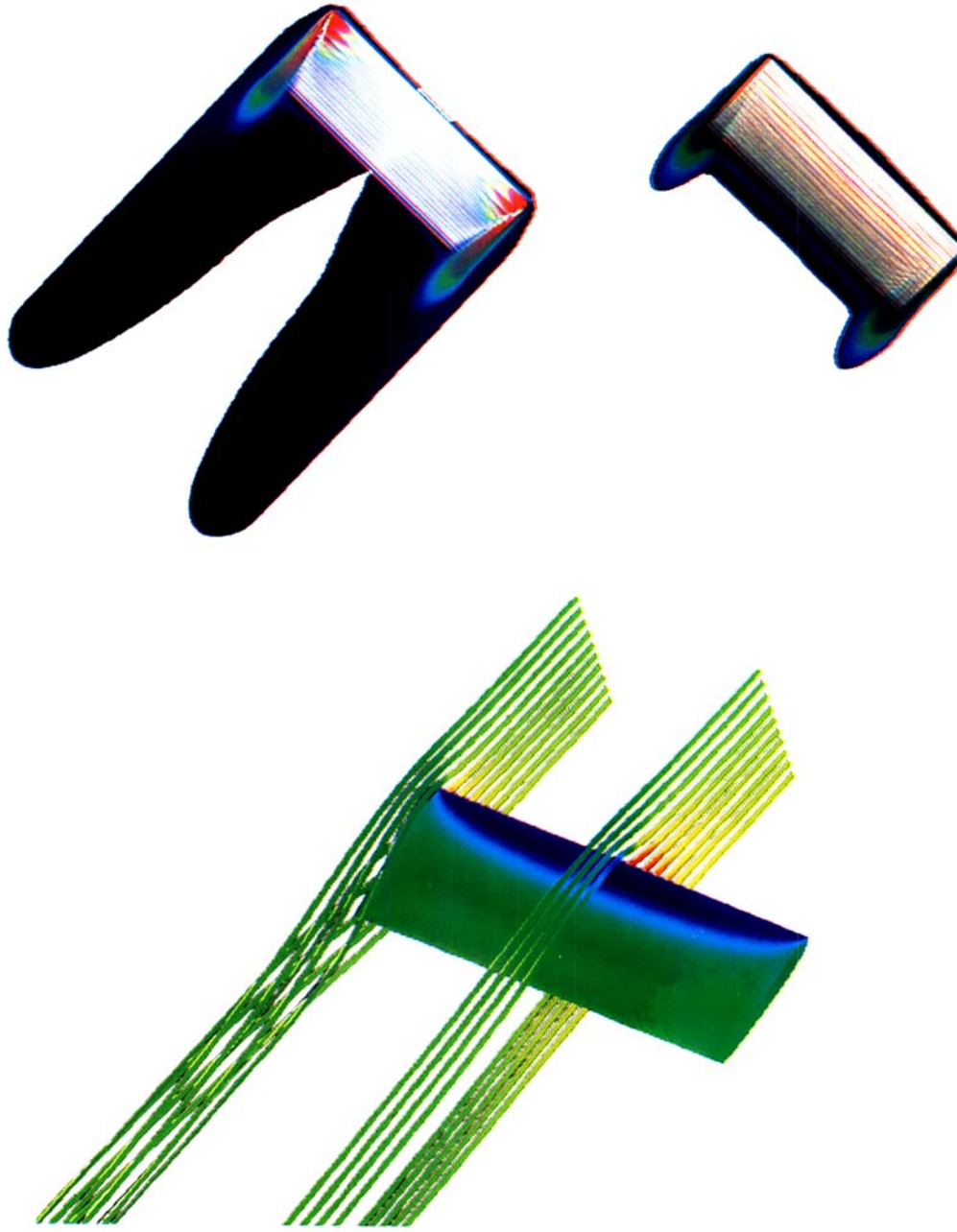

Plate 4. Flow past a stationary rectangular wing at $Re=10^7$: magnitudes of helicity (top left) and vorticity (top right), and pressure on the surface of wing along with two sets of stream ribbons colour coded with pressure (bottom)

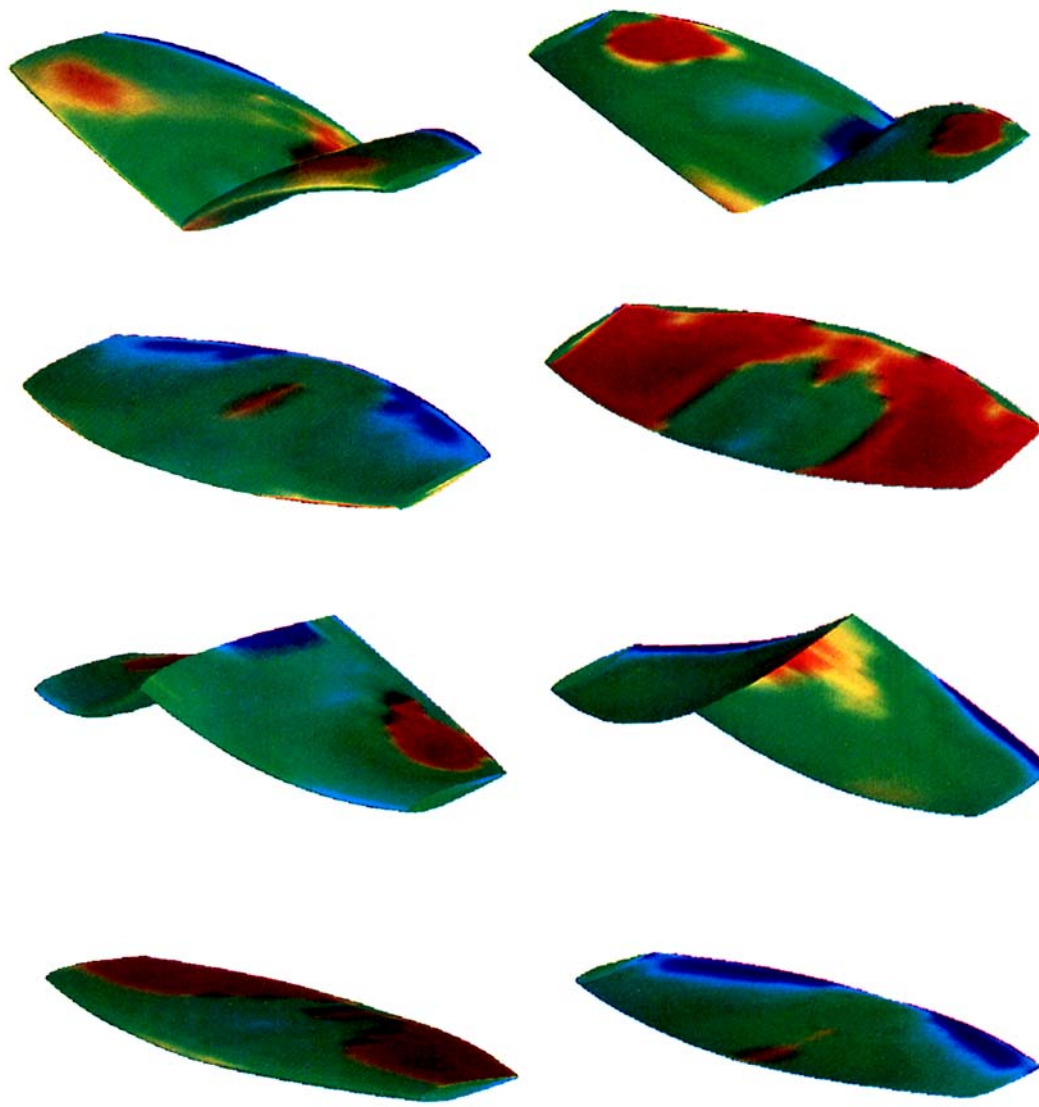

Plate 5. Flow past a flapping wing at *Re*=1000: Pressure on surface of wing during one period of motion. The left column shows the top view, while the right column shows the bottom view

3.2. The semidiscrete formulation for the pipe motion

We now describe the finite element formulation for the equation of motion for a flexible cantilevered pipe. We begin by defining the following finite element function spaces:

$$S^h = \left\{ \chi^h | \chi^h \in H^{2h}(\Omega), \chi^h(0, \theta) = \frac{\partial \chi^h}{\partial \zeta}(0, \theta) = 0 \right\}, \tag{29}$$

$$V^h = \left\{ w^h | w^h \in H^{2h}(\Omega), w^h(0) = \frac{\partial w^h}{\partial \zeta}(0) = 0 \right\}, \tag{30}$$

Here $H^2(\Omega)$ represents the finite-dimensional function space over the domain Ω formed by using, over the parent (element) domains, piecewise cubic Hermite shape functions.

The Galerkin formulations of (17) can be written as follows: start with

$$\chi^h(\zeta, 0) = \chi_0^h, \qquad \dot{\chi}^h(\zeta, 0) = \dot{\chi}_0^h; \tag{31}$$

given C_x, C_z, C_T, $\bar{u}$ and β, find $\chi^h \in S^h$ such that $\forall w^h \in V^h$

$$-\int_\Omega \frac{\partial^2 w^h}{\partial \zeta^2} \frac{\partial^2 \chi^h}{\partial \zeta^2} \mathrm{d}\Omega + \int_\Omega w^h \bar{u}^2 \left(-C_z \frac{\partial \chi^h}{\partial \zeta} + C_x + C_T \frac{\partial^2 \chi^2}{\partial \zeta^2} \right) \mathrm{d}\Omega - \int_\Omega w^h (1 - \beta) \frac{\partial^2 \chi^h}{\partial \theta^2} \mathrm{d}\Omega = 0. \tag{32}$$

The matrix form of the problem can be written as

$$\mathbf{Ma} + \mathbf{Cv} + \mathbf{Kd} = \mathbf{F}, \tag{33}$$

with the initial conditions

$$\mathbf{d}(0) = \mathbf{d}_0, \qquad \mathbf{v}(0) = \mathbf{v}_0, \tag{34}$$

where **M**, **C** and **K** are the mass, damping and stiffness matrices respectively, and **F** is the force vector. The vectors **a**, **v** and **d** correspond to the set of unknowns for the acceleration, velocity and displacement.

Time integration of the above set of equations is carried out by using the α-method proposed by Hilber *et al.*:[14]

$$\mathbf{Ma}_{n+1} + (1 + \alpha)\mathbf{Cv}_{n+1} - \alpha \mathbf{Cv}_n + (1 + \alpha)\mathbf{Kd}_{n+1} - \alpha \mathbf{Kd}_n = (1 + \alpha)\mathbf{F}_{n+1} - \alpha \mathbf{F}_n, \tag{35}$$

$$\mathbf{d}_{n+1} = \mathbf{d}_n + \Delta t \mathbf{v}_n + \frac{\Delta t^2}{2}[(1 - 2\eta)\mathbf{a}_n + 2\eta \mathbf{a}_{n+1}], \tag{36}$$

$$\mathbf{v}_{n+1} = \mathbf{v}_n + \Delta t[(1 - \gamma)\mathbf{a}_n + \gamma \mathbf{a}_{n+1}], \tag{37}$$

where the subscripts n and $n+1$ refer to evaluations at times t_n and t_{n+1} respectively. The values of the various parameters used in this scheme are

$$-\tfrac{1}{3} \leqslant \alpha \leqslant 0, \qquad \eta = (1 - \alpha)^2/4, \qquad \gamma = (1 - 2\alpha)/2. \tag{38}$$

For $\alpha = 0$ this scheme reduces to the trapezoidal scheme. It is well known that the trapezoidal scheme does not damp out the spurious high-frequency components. The α-method possesses improved algorithmic properties that can damp out any spurious participation of the higher modes. For our computations we set $\alpha = -0{\cdot}3$.

4. NUMERICAL EXAMPLES

4.1. *3D flow in a flexible cantilevered pipe*

In this fluid–structure interaction problem we simulate the 3D flow in a flexible cantilevered pipe and the response of the pipe to this flow. The deformation of the pipe is governed by the Bernoulli–Euler beam theory and this limits the reliability of our results to small deformations of the pipe. One of the quantities that characterizes the behaviour of the pipe–fluid system is the non-dimensional parameter β defined by equation (18). It relates the mass per unit length of the pipe to the mass per unit length of the fluid it is conveying. For a given value of β the pipe exhibits flow-induced oscillations if the flow velocity exceeds a certain critical velocity. At flow velocities less than the critical velocity all modes of the pipe oscillations are damped out. The dimensionless quantity used to parametrize the flow velocity is $\bar{u}$ and is defined by equation (19). We carried out computations for several values of $\bar{u}$ and β. In our computations the pipe has a unit diameter and the length-to-diameter ratio is 20. At the pipe inflow a paraboloid velocity field is specified. The Reynolds number based on the inflow velocity at the centreline and the pipe diameter is 1000. At the pipe exit we specify the fluid stress vector, with values corresponding to the inflow velocity profile. The initial condition for the simulation is the steady state flow in the pipe with the centreline deflection given by

$$\frac{x_0}{D} = 0{\cdot}1\frac{z^2}{3L^4}(z^2 - 4Lz + 6L^2), \tag{39}$$

where D is the diameter of the pipe.

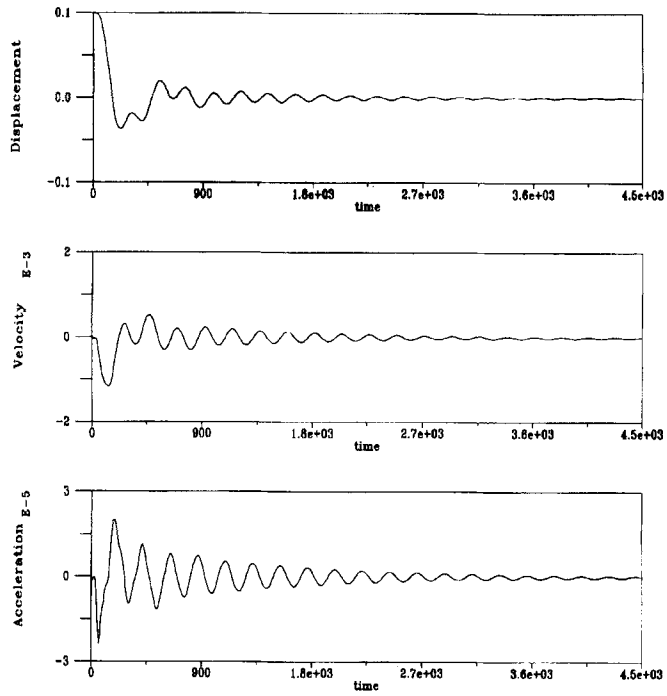

Figure 2. Flow in a flexible cantilevered pipe at $Re = 1000$, $\beta = 0{\cdot}05$ and $\bar{u} = 3{\cdot}5$: time histories of displacement, velocity and acceleration of free end of pipe

The initial velocity of the pipe is set to zero. The finite element mesh for the fluid flow computations consists of 20,449 nodes and 18,720 elements. At every time step 145,298 non-linear equations are solved to update the flow field. The computation of the deformation of the pipe involves the solution of 240 equations at every time step. The computations were carried out on the AHPCRC's CM-200.

$\beta = 0{\cdot}05$. The first set of computations was performed for $\bar{u} = 3{\cdot}5$. For this case, according to the experimental results reported by Gregory and Paidoussis,[9,10] all modes of the pipe oscillations should damp out and the pipe should eventually assume its undeformed shape. Figure 2 shows the time histories of the displacement, velocity and acceleration of the free end of the cantilevered pipe. We observe that, as expected, the amplitude of the pipe oscillations decays with time and eventually the pipe reaches its undeformed state.

Next we computed the response of the pipe for $\bar{u} = 4{\cdot}1$. Figure 3 shows the time histories of the displacement, velocity and acceleration of the free end of the cantilevered pipe. We observe that in this case the amplitude of the pipe oscillations increases with time, and eventually, the pipe exhibits temporally periodic oscillations. Figure 4 shows the pressure and lateral velocity in a cross-section of the pipe in its plane of motion during one period of the oscillations. Shown in Figure 5 are the displacement, velocity and acceleration along the pipe at three instants during half a period of the pipe oscillations. From these pictures we observe that the pipe exhibits the second mode of cantilevered beam oscillations.

$\beta = 0{\cdot}4$. For this value of β we again carry out computations for two different values of $\bar{u}$: 5·5 and 7·0. For the first case Figure 6 shows the time histories of the displacement, velocity and acceleration

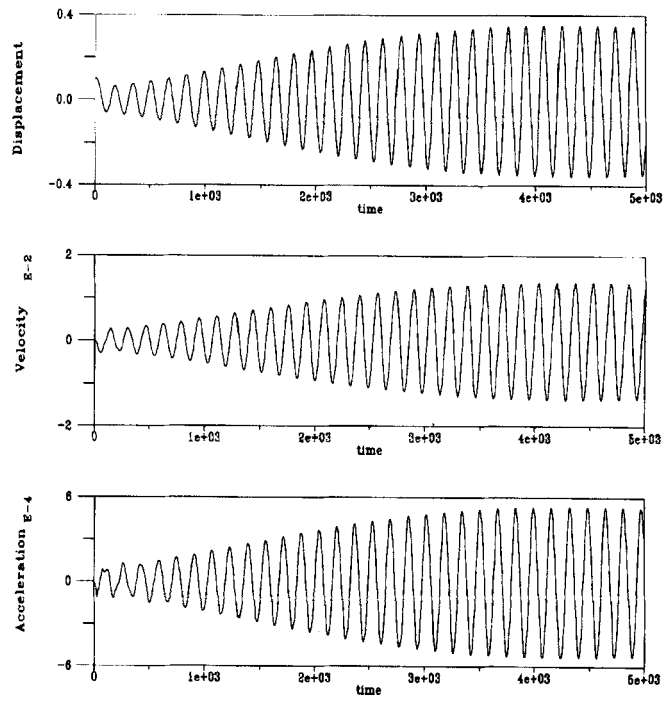

Figure 3. Flow in a flexible cantilevered pipe at $Re = 1000$, $\beta = 0{\cdot}05$ and $\bar{u} = 4{\cdot}1$: time histories of displacement, velocity and acceleration of free end of pipe

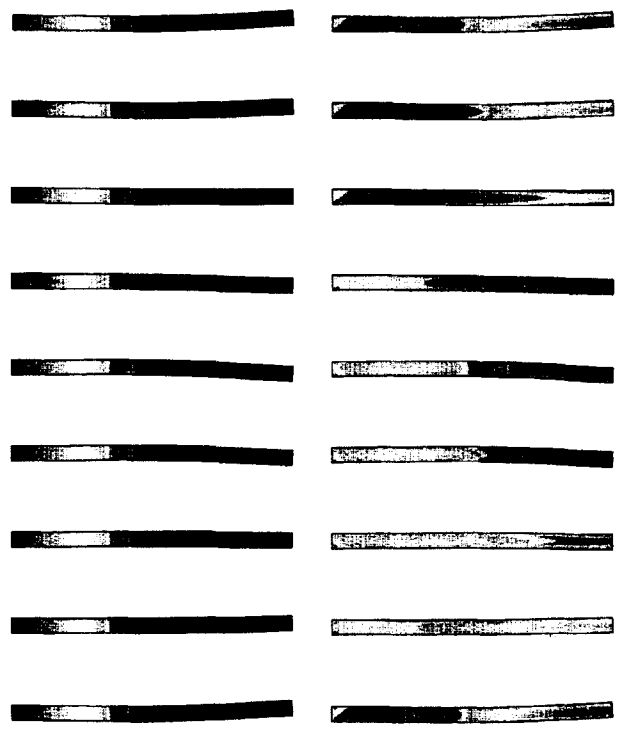

Figure 4. Flow in a flexible cantilevered pipe at $Re = 1000$, $\beta = 0{\cdot}05$ and $\bar{u} = 4{\cdot}1$: pressure (left) and lateral velocity (right) in cross-section of pipe in its plane of motion during one period of oscillations

of the free end of the cantilevered pipe. We observe that the amplitude of the pipe oscillations decays with time. Figure 7 shows the time histories of the displacement, velocity and acceleration of the free end of the cantilevered pipe for $\bar{u} = 7{\cdot}0$. We observe that the amplitude of the pipe oscillations increases with time and eventually the pipe exhibits a temporally periodic motion. Figure 8 shows the pressure and lateral velocity in a cross-section of the pipe in its plane of motion during one period of the oscillations. Shown in Figure 9 are the displacement, velocity and acceleration along the pipe at three instants during half a period of the pipe oscillations. From these pictures be observe that the pipe exhibits the second mode of cantilevered beam oscillations.

4.2. 3D flow past a rectangular wing at Reynolds number 1000, 2500 and 10^7

Here we compute the 3D flow past a fixed rectangular wing at 12·5° angle of attack. The wing has an aspect ratio of three and its cross-section is an NACA 0012 aerofoil with unit chord length. Since this problem does not involve any deforming domains, the computations are carried out by employing a semidiscrete version of the formulation described earlier in the paper. The centre of the rectangular wing is located at the origin of the computational domain. The upstream and downstream boundaries are located two and six chord lengths from the origin. The upper and lower boundaries are located at two chord lengths from the origin, while the side boundaries lie at three chord lengths from the origin. All three components of the velocity are specified at the upstream boundary. At the upper, lower and side boundaries the component of the velocity normal to these boundaries is specified to be zero, while the complementary components of the stress vector are set to zero. At the downstream boundary the

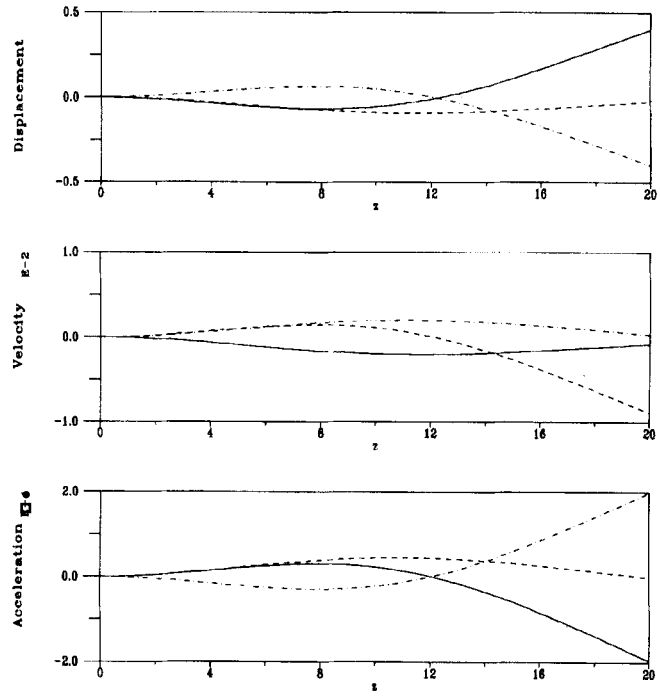

Figure 5. Flow in a flexible cantilevered pipe at $Re = 1000$, $\beta = 0{\cdot}05$ and $\bar{u} = 4{\cdot}1$: displacement, velocity and acceleration along pipe at three instants during half a period of pipe oscillations

stress vector is set to zero. The finite element mesh consists of 753,168 nodes and 727,552 hexahedral elements. At every time step 2,942,735 non-linear equations are solve to update the flow field. These equations are solved with matrix-free iterations. The computations were carried out on the AHPCRC's CM-5. On a 512-node CM-5 these computations achieved a sustained overall speed of 10 GFLOPS. The computation of the element-level residuals recorded a sustained speed of 16·8 GFLOPS. All computations are performed in double (64 bit) precision.

Laminar flow at Reynolds number 1000. At Reynolds number 1000 our computations converge to a steady state solution. This is in contrast with what one sees for a 2D simulation. For example, Mittal and Tezduyar[4] reported an unsteady 2D flow past an NACA 0012 aerofoil at 10° angle of attack at Reynolds number 1000. Plate 1 shows the volume rendering of the magnitudes of the helicity and vorticity around the wing. The presence of wing tip vortices can be easily observed from these images. These vortices are generated by the spillage of flow from the lower to the upper surface of the wing at the tips. It is our belief that it is because of these wing tip vortices that the vortex shedding is suppressed in flow past a wing. Perhaps one would be able to observe vortex shedding towards the centre of a wing with a larger aspect ratio. Plate 2 shows the pressure field in a plane passing through the centre of the wing. Shown in Figure 10 is an iso-surface of the streamwise component of velocity corresponding to 97·5% of the freestream value. Figure 11 shows the streamwise component of the velocity at two sections downstream of the wing. These pictures show details of the vortex roll-up in the wake of the wing. The aerodynamic coefficients we report are non-dimensionalized by the freestream dynamic pressure and the product of the wing span and chord length. The steady state drag and lift coefficients are 0·182 and 0·233 respectively.

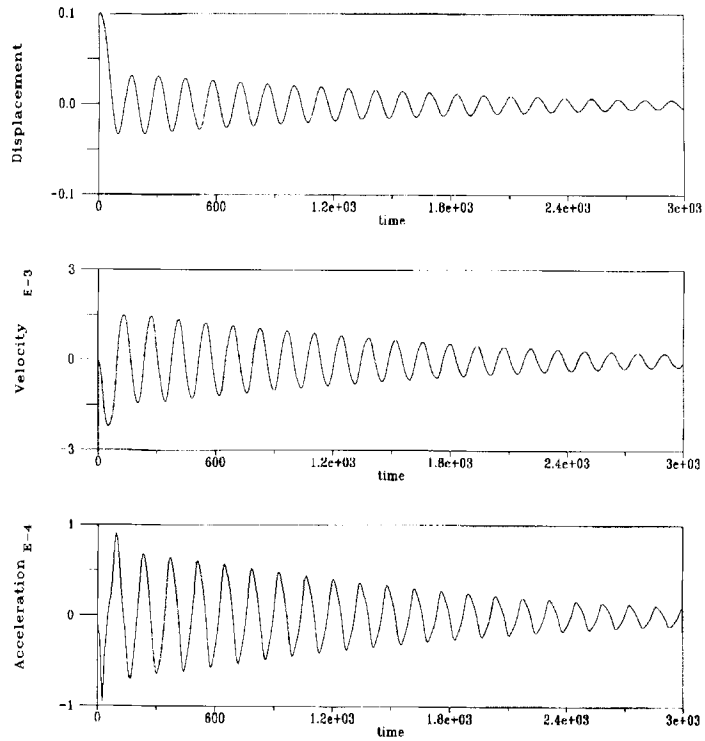

Figure 6. Flow in a flexible cantilevered pipe at $Re = 1000$, $\beta = 0{\cdot}4$ and $\bar{u} = 5{\cdot}5$: time histories of displacement, velocity and acceleration of free end of pipe

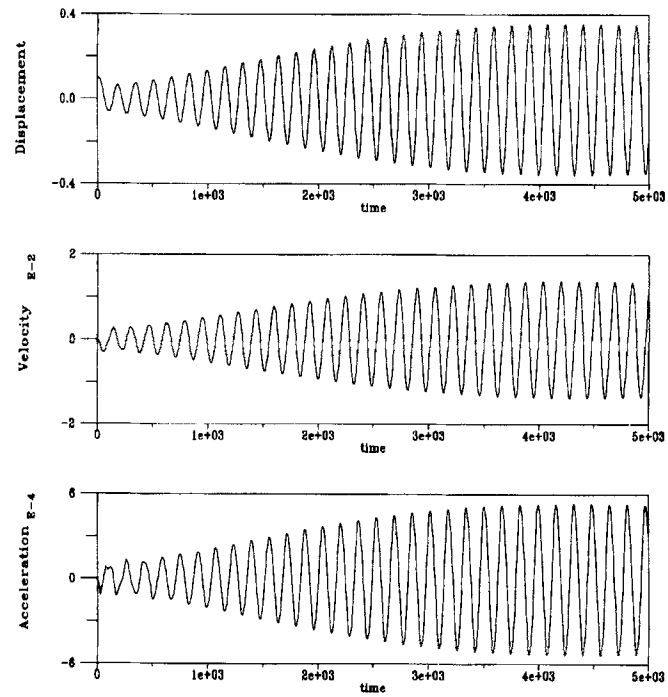

Figure 7. Flow in a flexible cantilevered pipe at $Re = 1000$, $\beta = 0{\cdot}4$ and $\bar{u} = 7{\cdot}0$: time histories of displacement, velocity and acceleration of free end of pipe

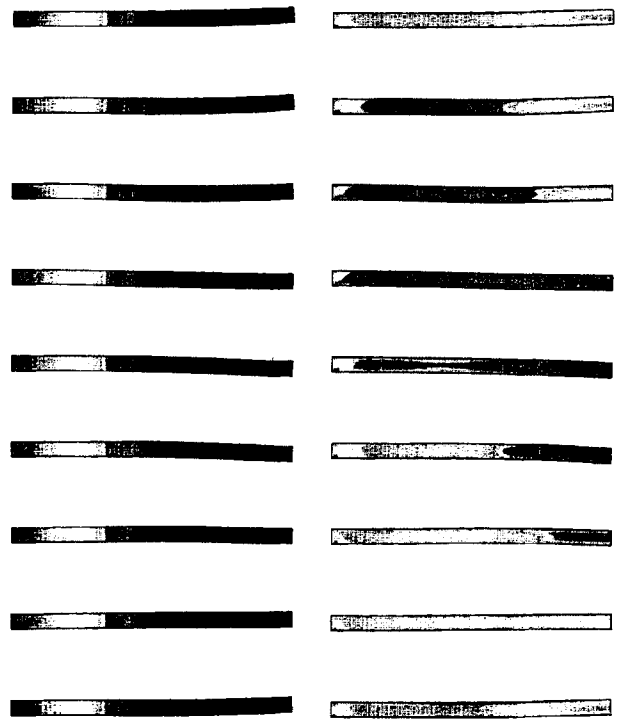

Figure 8. Flow in a flexible cantilevered pipe at $Re = 1000$, $\beta = 0{\cdot}4$ and $\bar{u} = 7{\cdot}0$: pressure (left) and lateral velocity (right) in cross-section of pipe in its plane of motion during one period of oscillations

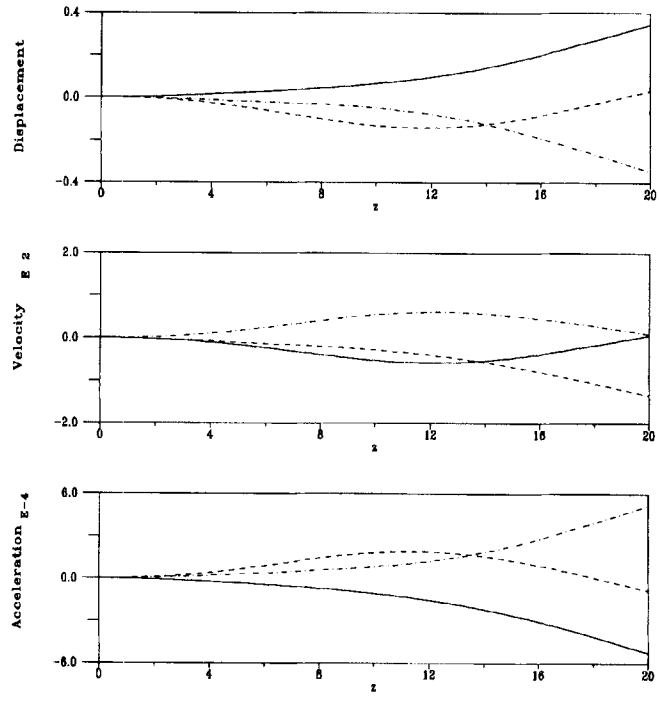

Figure 9. Flow in a flexible cantilevered pipe at $Re = 1000$, $\beta = 0{\cdot}4$ and $\bar{u} = 7{\cdot}0$: displacement, velocity and acceleration along pipe at three instants during half a period of pipe oscillations

Figure 10. Flow past a stationary rectangular wing at $RE = 1000$: iso-surface of streamwise component of velocity corresponding to 97·5% of freestream value

Laminar flow at Reynolds number 2500. The initial condition for this computation is the steady state flow past the wing at $Re = 2500$. Figure 12 shows the time histories of the aerodynamic coefficients for this simulation. We observe that the amplitude of the time-dependent components of these coefficients is much smaller than what one sees in 2D versions of similar flow problems. Figures 13 and 14 show the time histories of the three components of the velocity at two locations downstream of the wing. The point corresponding to Figure 13 is located towards the tip of the wing, whereas the one considered in Figure 14 lies more towards the mid-span. From these pictures we observe that the flow around the mid-span of the wing is more unsteady compared with the flow near the wing tip. The Strouhal number for the vortex shedding is 0·417. Plate 3 shows the volume rendering of the magnitudes of the helicity and vorticity at three different instants during half a period of the shedding. Again we observe the presence of wing tip vortices. Shown in Figure 15 is an isosurface of the streamwise component of velocity corresponding to 97·5% of the freestream value. It can be seen from this picture that the vortex shedding in this flow is confined to a region around the centre of the wing. Figure 16 shows the

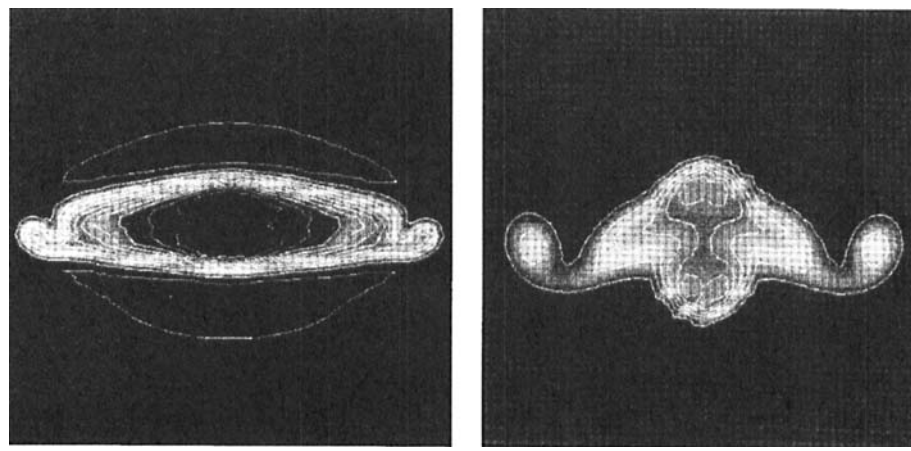

Figure 11. Flow past a stationary rectangular wing at $Re = 1000$: streamwise component of velocity at two sections downstream of wing. The image on the left is at the section one chord length downstream of the trailing edge, while the image on the right corresponds to a section close to the outflow boundary

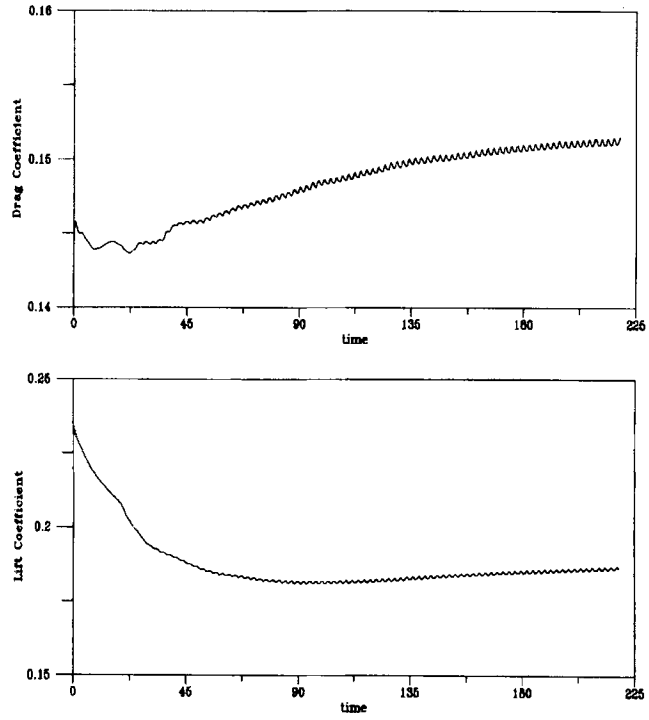

Figure 12. Flow past a stationary rectangular wing at $Re = 2500$: time histories of aerodynamic coefficients

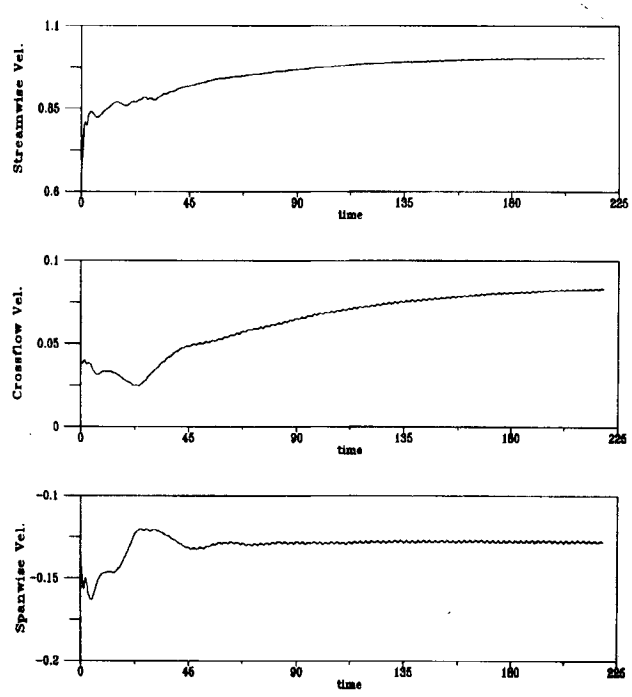

Figure 13. Flow past a stationary rectangular wing at $Re = 2500$: time histories of three components of velocity at a point near wing tip, downstream of wing. The location of the point relative to the centre of the wing is (0·62, − 0·14, − 1·47) chord lengths in the streamwise, crossflow and spanwise directions respectively

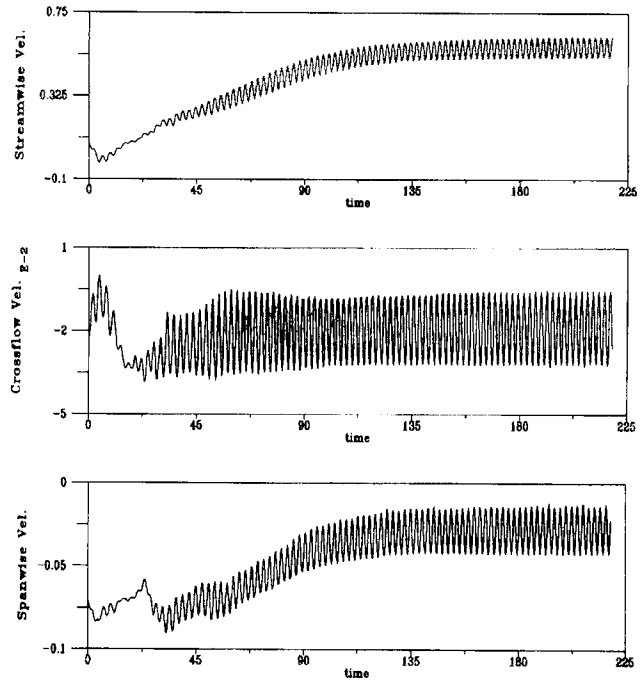

Figure 14. Flow past a stationary rectangular wing at $Re = 2500$: time histories of three components of velocity at a point near midspan, downstream of wing. The location of the point relative to the centre of the wing is (0·62, − 0·14, − 0·27) chord lengths in the streamwise, crossflow and spanwise directions respectively

Figure 15. Flow past a stationary rectangular wing at $Re = 2500$: iso-surface of streamwise component of velocity corresponding to 97·5% of freestream value

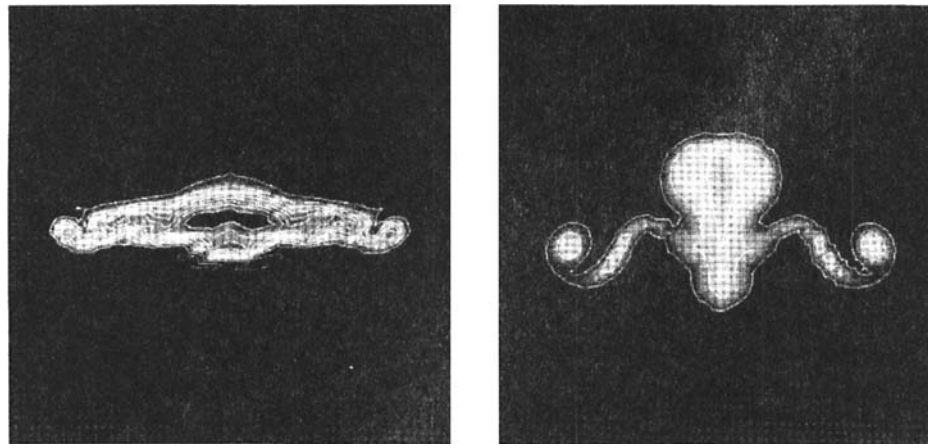

Figure 16. Flow past a stationary rectangular wing at $Re = 2500$: streamwise component of velocity at two sections downstream of wing. The image on the left is at the section one chord length downstream of the trailing edge, while the image on the right corresponds to a section close to the outflow boundary

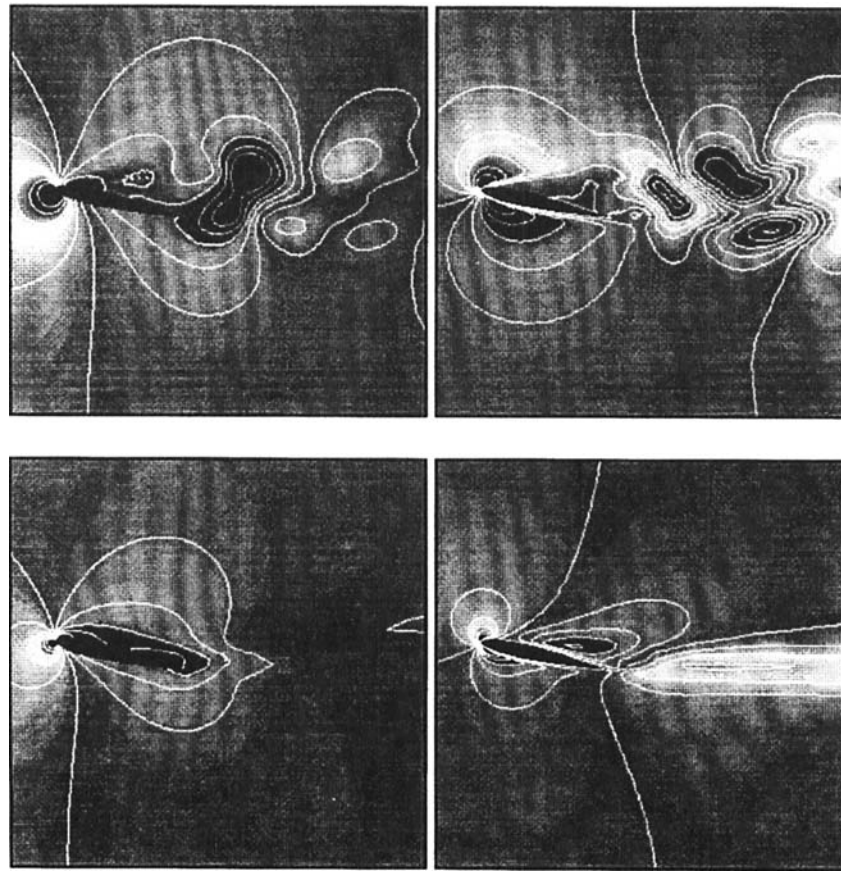

Figure 17. Flow past a stationary rectangular wing at $Re = 2500$: pressure (left) and crossflow velocity (right) at two sections along wing. The upper row shows the section at the centre of the wing, while the lower row shows a section near the wing tip

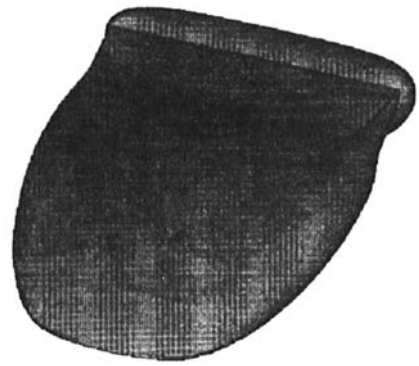

Figure 18. Flow past a stationary rectangular wing at $RE = 10^7$: iso-surface of streamwise component of velocity corresponding to 97·5% of freestream value

streamwise component of the velocity at two sections downstream of the wing. When we compare these pictures with the ones for Reynolds number 1000, we observe that the wing tip vortices are stronger at Reynolds number 2500. Figure 17 shows the pressure and crossflow velocity component at two sections along the wing. The upper row shows the section at the centre of the wing, while the lower row shows a section near the wing tip. We observe that the flow near the wing tips is steady, while vortex shedding takes place towards the mid-span.

Turbulent flow at Reynolds number 10^7. A simple algebraic turbulence model is used to compute the flow past the wing at Reynolds number 10^7. The Reynolds stress is modelled using a generalization of the Prandtl mixing length hypothesis.[17] In this model the kinematic viscosity ν is augmented by an eddy viscosity

$$\nu_T = (Kl)^2 \sqrt{[2\boldsymbol{\varepsilon}(\mathbf{u}) : \boldsymbol{\varepsilon}(\mathbf{u})]}, \tag{40}$$

where K ($=0{\cdot}41$) is the Von Karman constant and l is the shortest distance between the point of interest in the fluid and the solid wall.

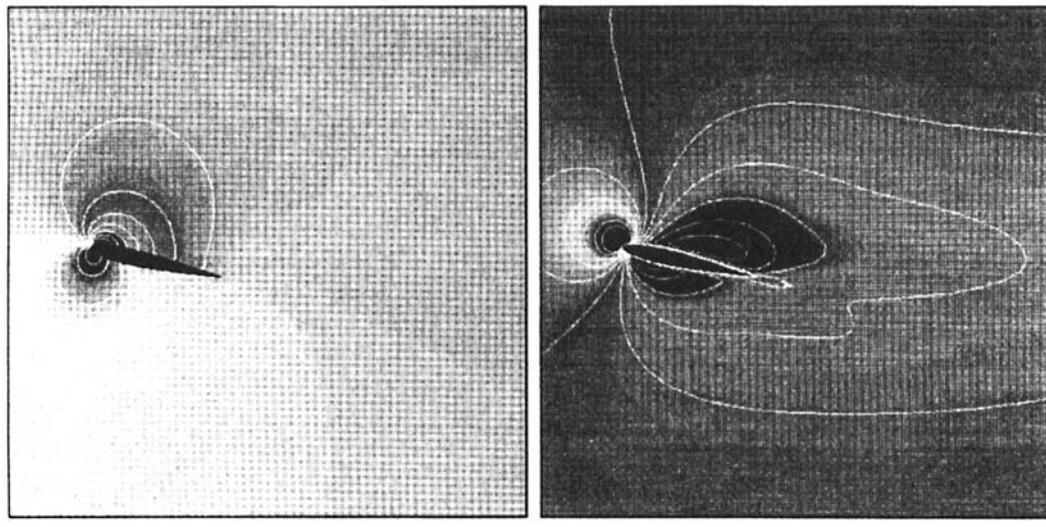

Figure 19. Flow past a stationary rectangular wing at $RE = 10^7$: pressure (left) and crossflow velocity (right) at a section passing through centre of wing

Plate 4 shows the volume rendering of the magnitudes of the helicity and vorticity, and the pressure on the surface of the wing along with two sets of stream ribbons colour coded with the pressure. We observe that the wing tip vortices are not as strong as they are in the case of laminar flow. It should be noted that the Prandtl mixing length hypothesis assumes that there are no regions of recirculation in the flow, so one should not expect accurate results in the wake and in the region of wing tip vortices. Shown in Figure 18 is an iso-surface of the streamwise component of velocity corresponding to 97·5% of the freestream value. Figure 19 shows the pressure and crossflow velocity at a section passing through the centre of the wing. The steady state drag and lift coefficients are 0·144 and 0·683 respectively, resulting in a lift-to-drag ratio of 4·7.

4.3. Flow past a flapping wing

In this problem we compute the flow past a wing in flapping motion. The length of the wing in the spanwise direction is 3·0. At the mid-span the chord length of the wing is unity and it tapers off quadratically to 0·5 at the tips. The cross-section of the wing is an NACA 0012 aerofoil. The centre of

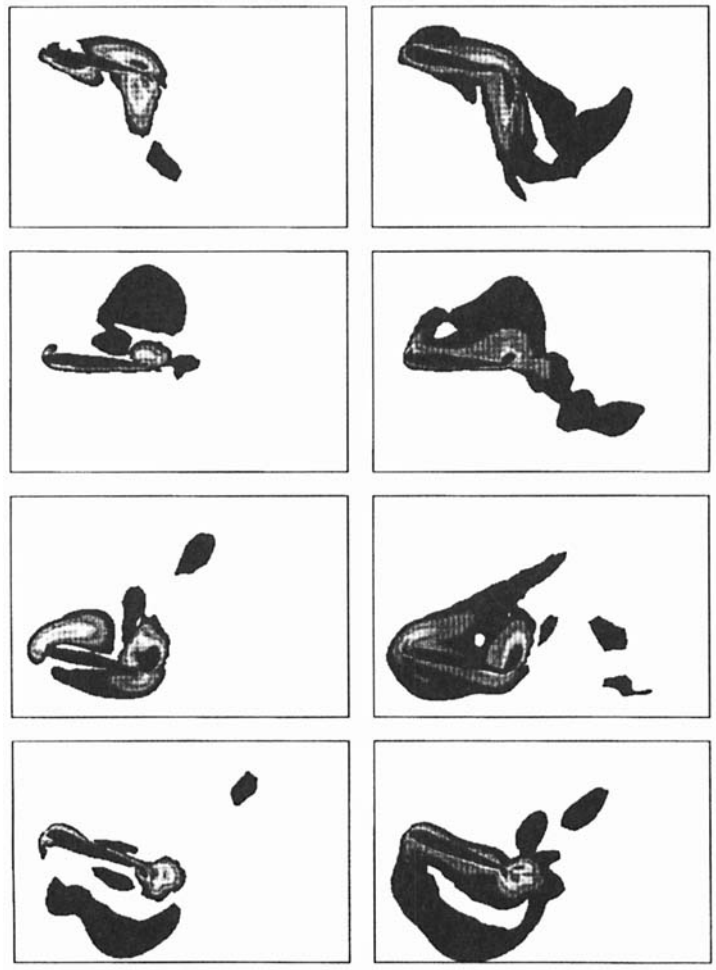

Figure 20. Flow past a flapping wing at $Re = 1000$: magnitude of helicity (left) and vorticity (right) at section midway between wing tip and centre of wing

the wing is located at the origin of a box whose downstream and upstream boundaries lie at eight and 16 units from the origin respectively. The upper and lower boundaries are located at eight units from the origin, while the side boundaries lie at 4·5 units from the origin. The finite element mesh consists of 145,402 nodes and 137,280 elements. At every time step 1,113,002 non-linear equations are solved to update the flow field. The computations were carried out on the AHPCRC's CM-5.

Let z be the axis along the wing span and y be the axis in the crossflow direction. The motion of the centreline of the wing along the span in the crossflow direction is given as

$$y = \cos\left(\frac{2\pi t}{T}\right)\left[0{\cdot}2 + \frac{0{\cdot}8}{b}\left(2|z| - \frac{2|z|}{b}\right)\right], \tag{41}$$

where b is the wing span and T is the period of the wing motion. In addition to this motion, the angle of attack varies as $12^\circ + 8^\circ \cos(2\pi t/T + \pi/2)$. This motion is based on the description given by Lighthill[15] of the flight of birds. A 2D version of a similar problem was reported by Johnson and Tezduyar.[18] The period of the wing motion in our computations is 2·0. This gives a dimensionless frequency, based on the chord length at mid-span and the freestream velocity, of 0·5. The Reynods number based on the freestream velocity and the chord length at mid-span is 1000. Plate 5 shows the pressure on the surface of the wing during one period of the motion. The left column shows the top view, while the right column shows the bottom view. Shown in Figure 20 are the magnitudes of the helicity and vorticity at a section 0·75 units from the centre of the wing. Figure 21 shows the time histories of the drag and lift coefficients for this simulation. We observe that during one period (the upstroke and downstroke) the motion of the wing generates a net thrust and lift.

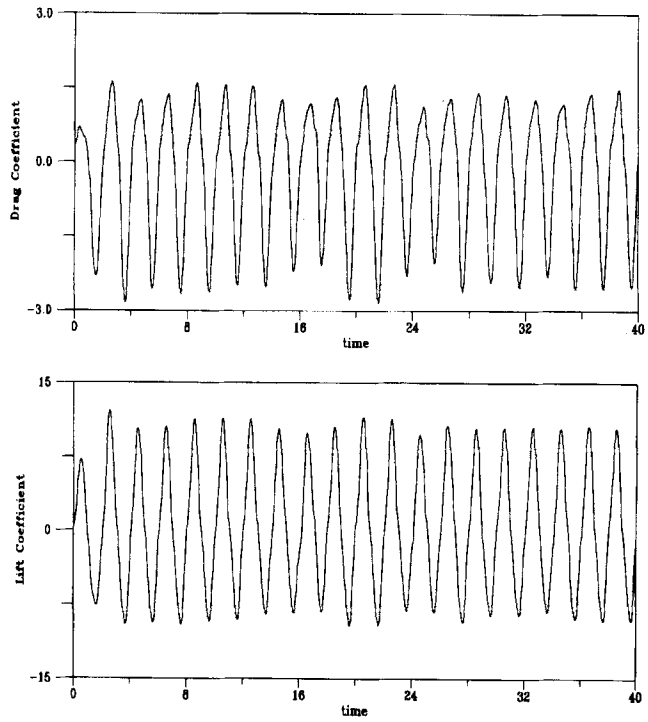

Figure 21. Flow past a flapping wing at $Re = 1000$: time histories of drag and lift coefficients

5. CONCLUDING REMARKS

Numerical results were presented for unsteady, 3D flows, including those involving fluid–structure interactions. These computations were carried out on the AHPCRC supercomputers CM-200 and CM-5, based on the massively parallel implementations of the stabilized space–time finite element formulation. The capability to solve 3D problems involving fluid–structure interactions was demonstrated by investigating the dynamics of a flexible cantilevered pipe conveying fluid. Good agreement with observations by other researchers was obtained. Computations of flow past a stationary rectangular wing confirmed the presence of wing tip vortices. An interesting pattern of vortex shedding was observed at Reynolds number 2500. Preliminary results were presented for flow past a wing in flapping motion. The use of a specially designed mesh-moving scheme in conjunction with the stabilized space–time formulation eliminates the need for remeshing, ensures high accuracy of the solutions and aids in the efficient utilization of the massively parallel computers.

ACKNOWLEDGEMENTS

This research was sponsored by NASA-JSC under grant NAG 9-449, by NSF under grant CTS-8796352, by ARPA under NIST contract 60NANB2D1272 and by ARO under grant DAAH04-93-G-0514. Partial support for this work has also come from ARO contract DAAL03-89-C-0038 with the AHPCRC at the University of Minnesota.

REFERENCES

1. T. E. Tezduyar, M. Behr and J. Liou, 'A new strategy for finite element computations involving moving boundaries and interfaces—the DSD/ST procedure: I. The concept and the preliminary numerical tests', *Comput. Methods Appl. Mech. Eng.*, **94**, 339–351 (1992).
2. T. E. Tezduyar, M. Behr, S. Mittal and J. Liou, 'A new strategy for finite element computations involving moving boundaries and interfaces—the DSD/ST procedure: II. Computations of free-surface flows, two-liquid flows, and flows with drifting cylinders', *Comput. Methods Appl. Mech. Eng.*, **94**, 353–371 (1992).
3. S. Mittal and T. E. Tezduyar, 'A finite element study of incompressible flows past oscillating cylinders and aerofoils', *Int. j. numer. methods fluids*, **15**, 1073–1118 (1992).
4. S. Mittal and T. E. Tezduyar, 'Massively parallel finite element computation of incompressible flows involving fluid–body interactions', *Comput. Methods Appl. Mech. Eng.*, **112**, 253–282 (1994).
5. M. Behr, A. Johnson, J. Kennedy, S. Mittal and T. E. Tezduyar, 'Computations of incompressible flows with implicit finite element implementations on the Connection Machine', *Comput. Methods Appl. Mech. Eng.*, **108**, 99–118 (1993).
6. Y. Saad and M. H. Schultz, 'A generalized minimal residual algorithm for solving nonsymmetric linear systems', *SIAM J. Sci. Stat. Comput.*, **7**, 856–869 (1986).
7. J. Kennedy, M. Behr, V. Kalro and T. E. Tezduyar, 'Implementation of implicit finite element methods for incompressible flows on the CM-5', *Comput. Methods Appl. Mech. Eng.*, **119**, 95–111 (1994).
8. G. W. Housner, 'Bending vibrations of a pipe line containing flow fluid', *J. Appl. Mech.*, **19**, 205–208 (1952).
9. R. W. Gregory and M. P. Paidoussis, 'Unstable oscillation of tubular cantilevers conveying fluid. I. Theory', *Proc. R. Soc. Lond. A*, **293**, 512–527 (1966).
10. R. W. Gregory and M. P. Paidoussis, 'Unstable oscillation of tubular cantilevers conveying fluids. II. Experiments, *Proc. R. Soc. Lond. A*, **293**, 528–542 (1966).
11. T. B. Benjamin, 'Dynamics of a system of articulated pipes conveying fluid. I. Theory', *Proc. R. Soc. Lond. A*, **261**, 457–486 (1961).
12. T. B. Benjamin, 'Dynamics of a syste mof articulated pipes conveying fluid. II. Experiments,' *Proc. R. Soc. Lond. A*, **261**, 487–499 (1961).
13. M. P. Paidoussis and N. T. Issid, 'Dynamic stability of pipes conveying fluid', *J. Sound Vibr.*, **33**, 267–294 (1974).
14. H. M. Hilber, T. J. R. Hughes and R. L. Taylor. 'Improved numerical dissipation for time integration algorithms in structural dynamics', *Earthq. Eng. Struct. Dyn.*, **5**, 283–292 (1977).
15. J. Lighthill, *An Informatl Introduction to Theoretical Fluid Mechanics*, Clarendon, Oxford, 1986.
16. T. E. Tezduyar, S. Mittal, S. E. Ray and R. Shih, 'Incompressible flow computations with stabilized bilinear and linear equal-order-interpolatin velocity–pressure elements', *Comput. Methods Appl. Mech. Eng.*, **95**, 221–242 (1992).
17. H. Schlichting, *Boundary Layer Theory*, transl. by J. Kestin, McGraw-Hill, New York, 1968.
18. A. A. Johnson and T. E. Tezduyar, 'Mesh update strategies in parallel finite element computations of flow problems with moving boundaries and interfaces', *Comput. Methods Appl. Mech. Eng.*, **119**, 73–94 (1994).